
Training distributed deep recurrent neural networks with mixed precision on GPU clusters.

Alexey Svyatkovskiy
Princeton University
Princeton, NJ 08540
alexey@princeton.edu

Julian Kates-Harbeck
Harvard University
Cambridge, MA 02138
jkatesharbeck@g.harvard.edu

William Tang
Princeton University
Princeton, NJ 08540
wtang@princeton.edu

Abstract

In this paper, we evaluate training of deep recurrent neural networks with half-precision floats. We implement a distributed, data-parallel, synchronous training algorithm by integrating TensorFlow and CUDA-aware MPI to enable execution across multiple GPU nodes and making use of high-speed interconnects. We introduce a learning rate schedule facilitating neural network convergence at up to $O(100)$ workers.

Strong scaling tests performed on clusters of NVIDIA Pascal P100 GPUs show linear runtime and logarithmic communication time scaling for both single and mixed precision training modes. Performance is evaluated on a scientific dataset taken from the Joint European Torus (JET) tokamak, containing multi-modal time series of sensory measurements leading up to deleterious events called plasma disruptions, and the benchmark Large Movie Review Dataset [1]. Half-precision significantly reduces memory and network bandwidth, allowing training of state-of-the-art models with over 70 million trainable parameters while achieving a comparable test set performance as single precision.

Keywords Neural networks, distributed computing, floating point precision.

1 Introduction

Training deep neural networks is a computationally intensive problem which requires engagement of high-performance computing (HPC) clusters. Several implementations of distributed Stochastic Gradient Descent (SGD) exist, exploiting general-purpose hardware (CPU [2] and GPU [3]) as well as FPGA [4].

Data-parallel distributed training algorithms keep a copy of an entire neural network model on each worker, processing different mini-batches of the training dataset on each in parallel lock step. Some advantages of using synchronous SGD implementations are a reliable model convergence, ease of debugging, and avoidance of stale gradients. When training state-of-the-art large models (with over $O(10^7)$ trainable parameters [5]) the net gradient size per iteration can reach up to a few GB, potentially exceeding the limits of the network data transfer rate (network bandwidth) or the GPU device memory.

It has been shown that deep convolutional and recurrent neural networks allow using lower precision at both the training and inference stages in application to image classification and language modeling tasks [6, 7, 8]. Nevertheless, no extensive studies have been performed for recurrent neural networks during distributed training, which are at the focus of this paper.

Compared to single precision, using half-precision floats allows training models with twice as many parameters, improves the maximum computational throughput, and optimizes memory and network bandwidths. At the time of writing, half-precision computation is supported by GPUs only, while the latest generation of Intel CPUs (e.g. Haswell, Broadwell) provide a capability for converting between single and half floating point precisions in hardware by means of the F16C instruction set.

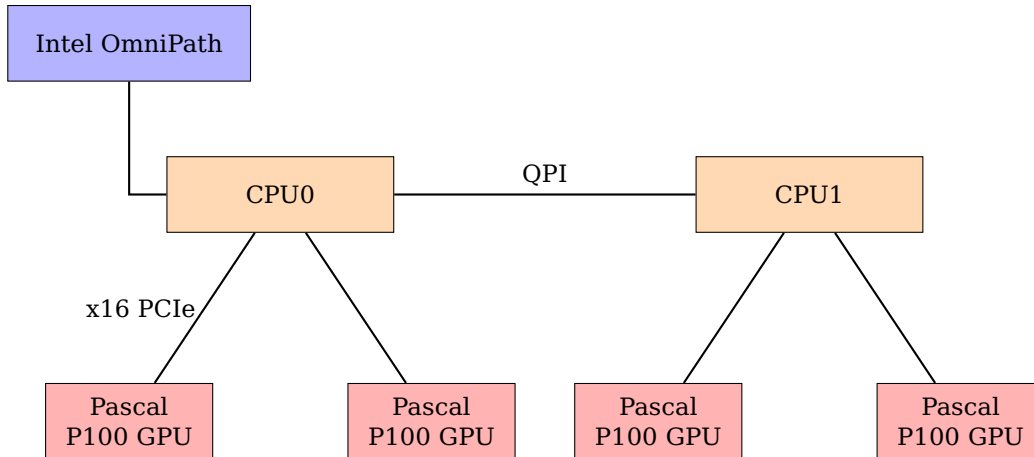


Figure 1: Hardware architecture layout of the Tiger cluster node.

A set of strong scaling tests is performed using a framework integrating TensorFlow [9] with custom parameter averaging and global weight update routines implemented with CUDA-aware MPI. The software stack makes use of CUDA 8, GPU accelerated deep learning primitives from CuDNN 6, and TensorFlow 1.3. The performance is reported on a scientific dataset taken from the JET tokamak – the largest operating tokamak in the world [10] – comprising over 4000 time series, some of which result in deleterious events called plasma disruptions. The time series contain multi-modal sensory measurements, including both scalars and one-dimensional arrays, collected with a sampling rate of 1 ms. The description of the JET dataset is provided in Appendix A.1.

In addition to the JET dataset, we repeat the calculation on the Large Movie Review Dataset (IMDB) [1], which is a public dataset often used for sequence learning and time-series forecasting tasks in deep learning community.

Following [11], our goal is to train the recurrent neural net to predict the onset of a disruption at least 30 ms in advance of the actual event. This is the time that would be required to implement mitigation strategies (such as rapid neutral gas injection) in a real experiment after receiving an alarm. The nature of the problem of disruption forecasting in tokamak fusion plasmas makes long short-term memory (LSTM) networks a promising candidate.

The paper is organized as follows: we start with the hardware specifications and an overview of recurrent neural networks in the Sections I and II; Section III describes the details of the distributed training algorithm implemented in the framework; Section IV evaluates training with half-precision floats; Section V summarizes the performance on the plasma disruption dataset from JET. Section VI concludes the paper.

2 Hardware specifications

Scaling tests are performed on the Dell Linux cluster at Princeton University named "Tiger". It has a theoretical peak performance exceeding 27 petaflops, which is delivered by 320 NVIDIA Pascal P100 GPUs across 80 Intel Broadwell nodes. Each GPU is mounted on a dedicated x16 PCI express bus with 16 GB of HBM2 memory as shown in Fig. 1. The nodes of the cluster are interconnected by an Intel Omnipath high-speed interconnect. The CPUs are Intel Broadwell E5-2680v4 with 28 cores per node.

3 Neural Network architecture

Recurrent Neural Networks (RNN) are a family of neural networks capable of processing sequential data of arbitrary length. Long short-term memory networks (LSTM) [12], a particularly successful form

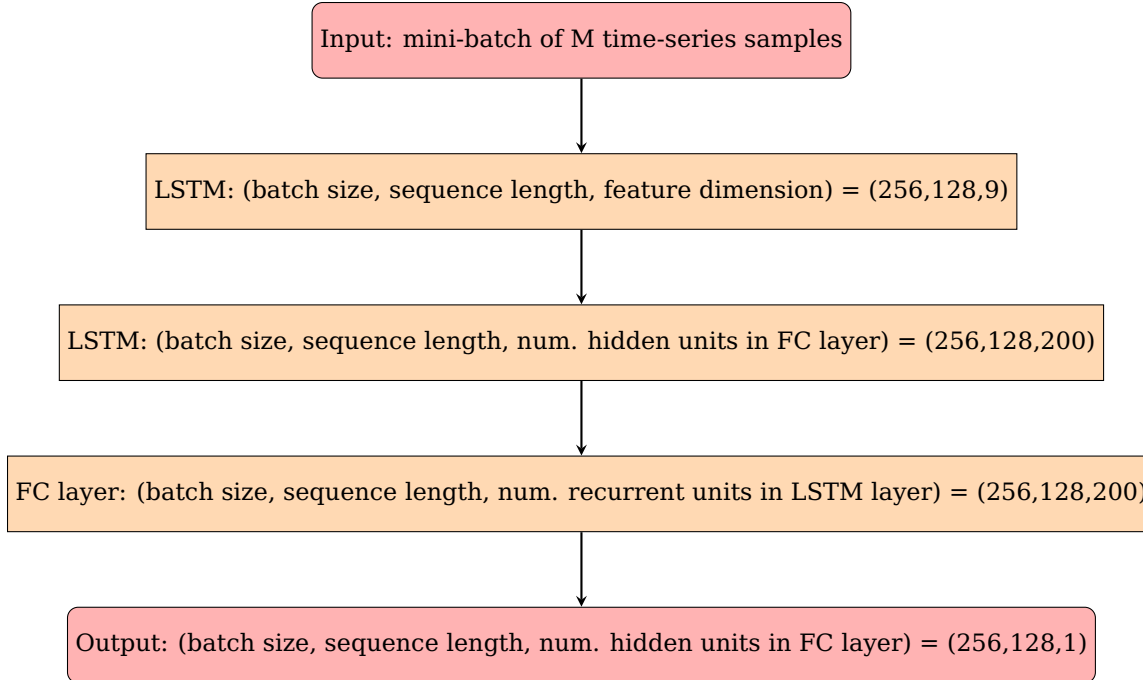


Figure 2: A typical neural network architecture for plasma disruption forecasting task.

of RNNs, trained on large datasets can obtain remarkable performance results across a wide variety of domains – from image captioning [13], to sentiment analysis and machine translation [14, 15].

A LSTM unit uses no activation function within its recurrent components. Thus, the stored values are not iteratively expanded or squeezed over time, and the gradient does not tend to explode or vanish when trained. Instead, LSTMs contain gates controlling information flow, which are implemented using the logistic function.

A typical neural network architecture for plasma disruption forecasting involves LSTMs and fully connected layers which are illustrated in Fig. 2. Here, each LSTM layer has 200 hidden units, with application of L2 regularization and recurrent dropout. Fully connected layers with ReLU activation are applied for each temporal slice $t = 0 \dots 128$. Tunable parameters of neural network are determined via random search hyperparameter optimization.

Neural networks are trained iteratively, making multiple passes over an entire data set before converging to a minimum. Each training iteration includes the forward propagation (**fprop**), loss calculation, backpropagation (**bprop**) followed by the weight update. Backpropagation through time (BPTT) is a gradient-based neural network training algorithm applied to train RNNs and LSTMs.

4 Distributed computing framework

We implement a distributed computing framework making use of TensorFlow for layer definitions, **fprop** and **bprop** steps, and a custom global weight update routine with parameter averaging implemented using CUDA-aware MPI to take advantage of high-speed network interconnects like OmniPath or Infiniband on HPC clusters, as well as the GPU-direct technology.

The following summarizes the implementation of distributed data-parallel synchronous stochastic gradient descent with parameter averaging:

1. Initialize the network parameters randomly based on the model configuration
2. *broadcast* a copy of the current parameters to each worker
3. Perform **fprop** and **bprop** passes on each worker using a mini-batch m_i of data

4. Aggregate gradients from each worker using *allreduce*, then average them on worker with task 0 to obtain global raw gradients
5. Update optimizer internal state and global weights using this global gradient on worker with task 0
6. *broadcast* global parameters after update back to all workers, return to the step (2) and repeat for mini-batch m_{i+1} of data

Aggregating raw gradients allows using any optimizers in step (5), making the framework more flexible. In this paper, we focus on the stochastic gradient descent optimizer with momentum, which is given by the following update equations:

$$H_k = m \cdot H_{k-1} - \lambda \Delta W, \tag{1}$$

$$W_k = W_{k-1} + H_k \tag{2}$$

With the above approach, the master has to collect all N gradients in lock-step. An alternative, fault tolerant approach requires collecting a fraction of gradients (normally at 90-95%) before proceeding to averaging, thus avoiding stalling the calculation in case of a slow node or a node failure.

5 Learning rate schedule

The learning rate controlling magnitude of the weight update during stochastic gradient descent in Eq. 1 is lowered upon completion of each epoch. We use exponential learning rate schedule given by the following equation:

$$\lambda_i = \lambda_0 \cdot \gamma^i \tag{3}$$

where λ_0 is the base learning rate, γ is the learning rate decay constant, and i is the epoch number.

In a distributed regime, the learning rate is adjusted to facilitate reliable model convergence. First, the base learning rate is reduced as the number of workers N increases:

$$\lambda_0(N, n) = \frac{\lambda_0}{1.0 + \frac{N}{n}} \tag{4}$$

here, parameter n controls the base learning rate adjustment, and is equal to the number of workers at which it is halved.

Secondly, the effective base learning rate, which is defined as a product of the number of workers and the base learning rate - $\lambda_0 \cdot N$ - is clipped if it exceeds the maximum value of 0.1.

Fig. 3 shows validation level AUC per epoch calculated at single precision for up to 100 worker GPUs. While keeping batch size β_0 and base learning rate λ_0 the same in all cases, the number of workers has been varied. Effective batch size of the ensemble of workers is proportional to the number of workers: $\beta = N \cdot \beta_0$. Consequently, the model convergence may be affected for large ensemble sizes. As seen, the learning rate schedule introduced in Seq. 5 facilitates neural network convergence when training with up to 100 worker GPUs, achieving comparable AUCs at the plateau.

6 Half-precision training modes

Floating point formats consist of a sign, an exponent, and a mantissa. We use the single precision floating point format (**FP32**, 23-bit mantissa and 8-bit exponent) as a reference because this is the most widely used format in deep learning, especially for GPU computation. Half-precision floating point format (10-bit mantissa and 5-bit exponent) has a numerical range of (0.00006,65504). This narrow numerical range can potentially result in an overflow ("Inf/NaN" problem) or an underflow ("vanishing gradient") during training of neural networks.

We show that the **FP16** with loss scaling has no significant impact on the neural network model convergence, resulting in an accuracy comparable to the **FP32** baseline, while allowing to train models with larger number of parameters, improving throughput and memory use.

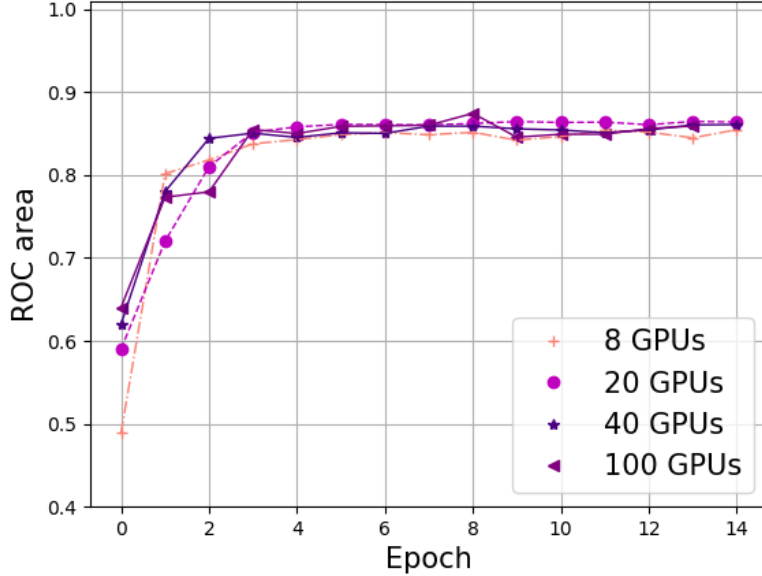


Figure 3: Validation level AUC per epoch calculated at single precision for 8, 20, 40 and 100 worker GPUs. Base learning rate: $\lambda_0 = 0.0004$, batch size: $\beta_0 = 256$. SGD optimizer with momentum, loss scaling factor: 10.0.

To enable **FP16** training, a custom MPI data type of 2 contiguous bytes and a reduction operation (namely *allreduce*) have been implemented.

We distinguish the following precision modes:

1. Math: matrix and element-wise multiplication during forward and backward passes
2. Synchronization: parameter averaging; precision of weights and gradients sent across network
3. Weight update

The baseline for the comparisons is the case when all – math, synchronization and the weight update – are of single precision.

The parts of the deep learning framework which are executed on CPU (including data preprocessing and normalization) all rely on the **FP32** and would not benefit from **FP16**, as the half type is currently emulated on CPU by converting the 32-bit floating point representations into a 16-bit floating point representation, thus leading to significantly slower runtimes.

7 Performance evaluation

The total time to process a mini-batch of data during synchronous SGD can be divided into computation T_{batch} and synchronization T_{sync} times. With the data-parallel implementation, computation time per mini-batch step remains constant in the number of workers, $T_{batch} \sim const$. Synchronization between workers is performed by means of a tree-like native MPI *allreduce* operation, yielding logarithmic complexity $T_{sync} \sim \log(N)$ — providing a major benefit over the parameter server approach often used in distributed training. The amount of data processed during one mini-batch step increases linearly with the number of workers N . Thus, the number of mini-batches (and consequently the total time T_{epoch}) required for an epoch decreases linearly with N .

$$T_{epoch} \propto \frac{1}{N}(T_{batch} + T_{sync}) = \frac{1}{N}(A + B \cdot \log(N)) = O\left(\frac{\log(N)}{N}\right) \quad (5)$$

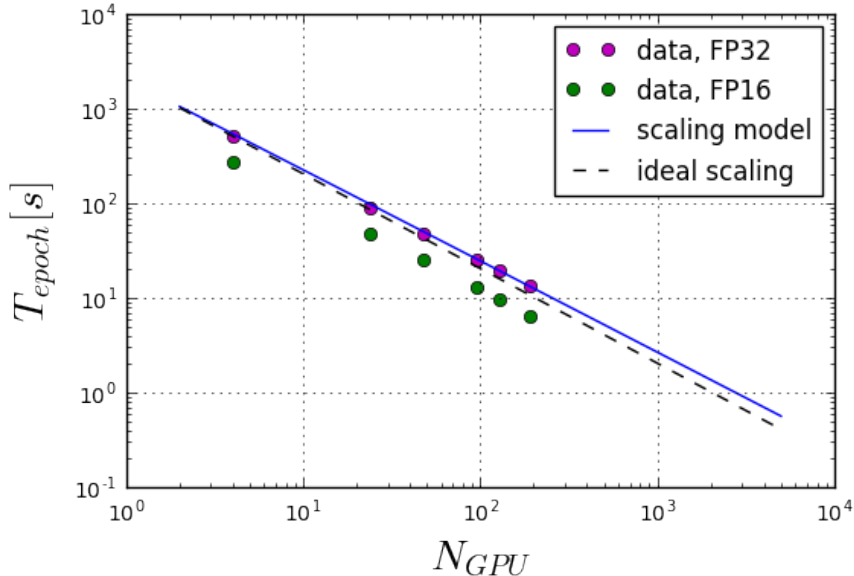


Figure 4: Compute time per epoch as a function of the number of worker GPUs for **FP16** and **FP32** at a maximum processing rate.

Fig. 4 shows the compute time per epoch as a function of the number of worker GPUs for **FP16** and **FP32** during distributed training on Pascal P100 GPUs at the maximum processing rate. As seen, the training algorithm provides linear runtime scaling as the number of worker GPUs N increases.

The LSTM outputs a plasma disruptivity signal which is counted as an alarm when it passes a user-defined threshold. Calling an alarm at any point during a non-disruptive shot counts as a false positive (FP). Calling an alarm before the 30 ms cutoff during a disruptive shot counts as a true positive (TP). The objective of optimization is to maximize true positives while minimizing false positives. Naturally, a higher threshold will lead to less alarms, and thus less false positives but also less true positives. Varying the threshold traces out an ROC curve that captures the full trade-off between TPs and FPs. The validation level area under the ROC curve, or AUC (area under curve), is the figure of merit we chose to characterize the quality of a given binary predictor, and applicability of the half-precision training.

As seen in Fig. 5, both **FP16** and **FP32** show AUC as a function of epoch of similar shapes, reaching the plateau at around AUC=0.87 by the epoch 6. The test set AUC values are 0.96 ± 0.03 for both the **FP16** and **FP32** calculations, with the corresponding test ROC curves shown in Fig. 6. The test data set is obtained from a different physical configuration leading to the difference between validation and test performances.

In a separate experiment, where neural network was trained till full convergence determined by "early stopping" with the validation AUC as a monitored quantity it took 8 and 9 passes over the training dataset to complete the training in the case of **FP16** and **FP32** respectively.

The consistent accuracies between baseline and half-precision runs are achieved by applying a scalar multiplier α to the loss function before evaluating partial derivatives on the **bprop** step. For hinge loss function with t denoting a classification label and y the predicted neural network outcome we get:

$$L(y) = \alpha \cdot \max(0, 1 - t \cdot y). \quad (6)$$

The neural network training experiment is repeated on the benchmark IMDB dataset at different floating point precisions and learning rates. As seen in Fig. 7, both **FP16** and **FP32** show AUC as a function of epoch of similar shapes, reaching the plateau at around AUC=0.86 by the epoch 9 at $\lambda_0 = 0.02$ and epoch 6 at $\lambda_0 = 0.05$.

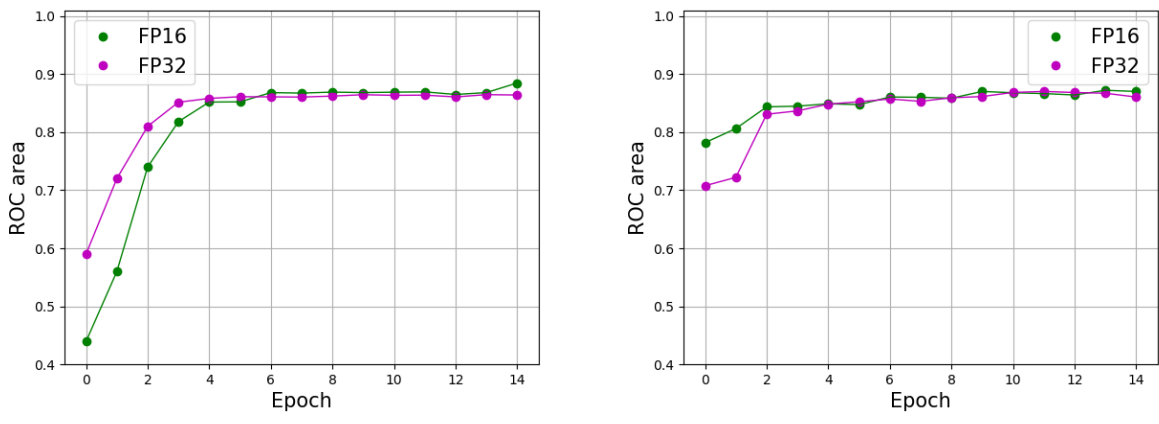


Figure 5: Validation level AUC per epoch calculated for **FP16** and **FP32** precisions. Left: base learning rate $\lambda_0 = 0.0004$, right: base learning rate $\lambda_0 = 0.001$. SGD optimizer with momentum, loss scaling factor: 10.0.

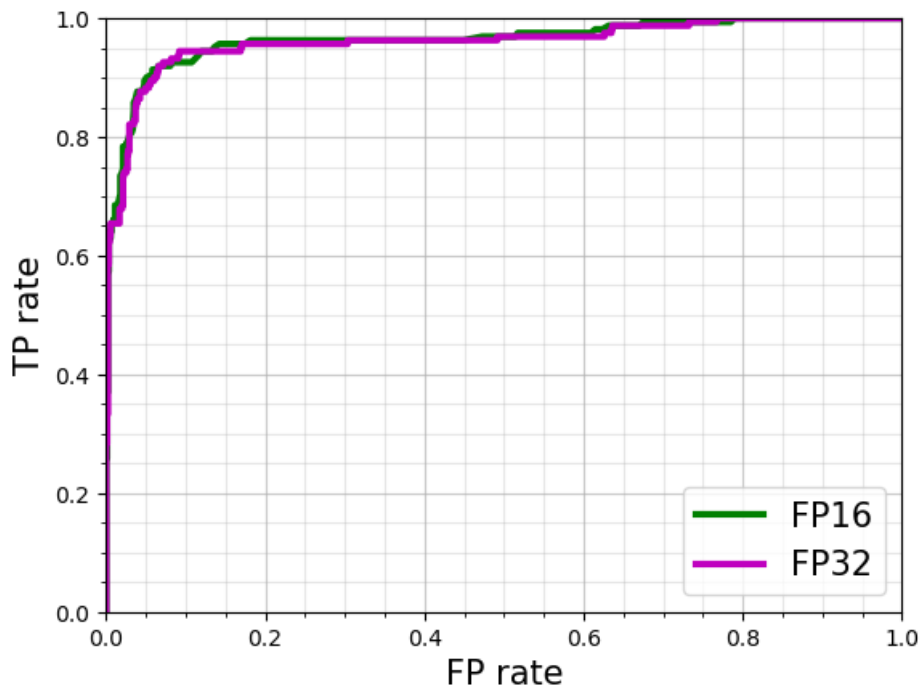


Figure 6: Test level ROC curve calculated for **FP16** and **FP32** precisions.

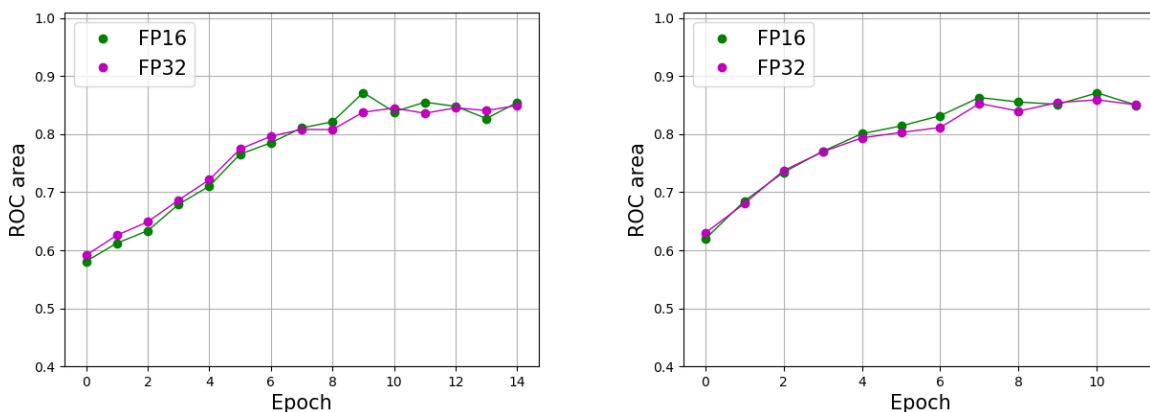


Figure 7: Validation level AUC per epoch calculated for **FP16** and **FP32** precisions for the Large Movie Review Dataset. Left: base learning rate $\lambda_0 = 0.02$, right: base learning rate $\lambda_0 = 0.05$.

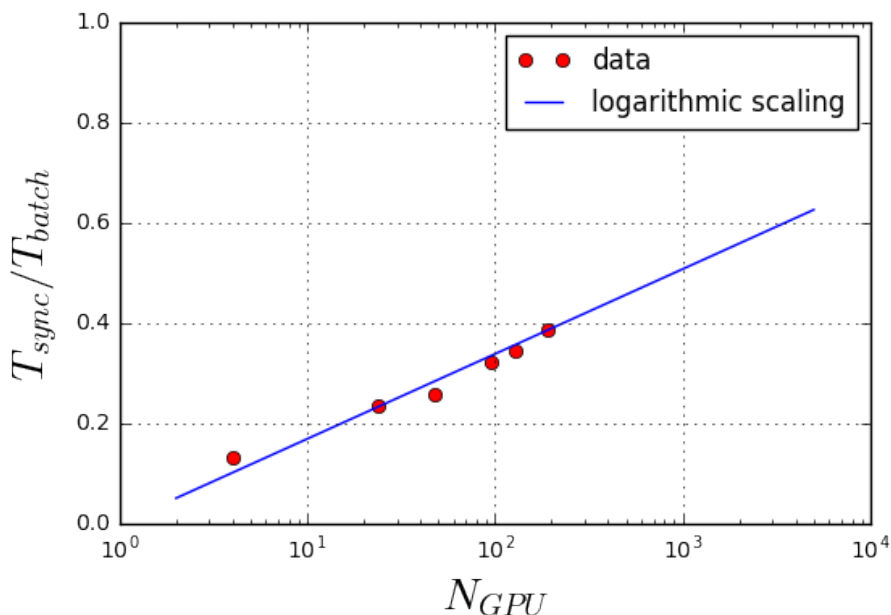


Figure 8: Ratio of synchronization to computation time per mini-batch as a function of the number of worker GPUs.

Fig. 8 shows the ratio of synchronization time to computation time (each per mini-batch) as a function of the number of workers when training on Pascal P100 GPUs. As seen, communication time during the distributed training follows logarithmic scaling up to an $O(100)$ worker GPUs.

Lower floating point precision allows training deeper models in a data-parallel fashion, and, potentially, use larger batch sizes. Tab. 3 summarizes the maximum number of trainable parameters and number of layers for different floating point precisions and batch sizes. The model capacity is increased by stacking LSTM layers, while keeping the number of recurrent units and a sequence length fixed.

The net gradient corresponding to the models in Tab. 3 can be estimated as $N_{par} \cdot \text{Batch size} \cdot \text{Size of datatype}$, comprises 9.4 GB/iter . Using MPI *allreduce* for synchronization, each GPU must send and receive about 9.4 GB of data. Using the CUDA-aware MPI implementation (such as OpenMPI) allows data transfers between GPUs using GPUDirect random direct memory access with a bandwidth of

Precision	N_{par}	N_{layers}	Batch size
FP64	$4.6 \cdot 10^6$	15	256
FP32	$9.2 \cdot 10^6$	29	256
FP16	$18.2 \cdot 10^6$	58	256
FP64	$18.2 \cdot 10^6$	58	64
FP32	$36.3 \cdot 10^6$	118	64
FP16	$72.1 \cdot 10^6$	234	64

Table 1: Maximum capacity of the model in terms of number of trainable parameters, batch size, and equivalent model depth fitting in Pascal P100 GPU device memory for half-precision, single precision, and double floating point precision. A tuned configuration of the neural network for the plasma disruption forecasting task [11] consisting of 200 recurrent units and the sequence length of 128 is used.

roughly 10 GB/s, however, with the high-speed Intel Omnipath interconnect in our cluster the data can be transferred across the network with a bandwidth of 6.25 GB/s, which is slower. Since the limiting factor is the network communication, a single iteration requires about:

$$\frac{\text{Net gradient size}}{\text{Bandwidth}} = \frac{9.4 \text{ GB/iter}}{6.25 \text{ GB/s}} \approx 1500 \text{ ms/iter} \quad (7)$$

8 Conclusions

Training of deep recurrent neural networks with half-precision floats has been evaluated on a computing framework integrating TensorFlow with custom parameter averaging and global weight update routines implemented with CUDA-aware MPI. Tests with the JET plasma disruption time series dataset, and the benchmark Large Movie Review Dataset (IMDB) yield comparable validation level performances at the end of each epoch for half and single floating point precisions.

A distributed data-parallel synchronous stochastic gradient descent approach showing strong nearly linear $O(\frac{\log(N)}{N})$ runtime scaling is run on GPU clusters and evaluated. With half-precision runs, memory bandwidth and communication overhead is significantly reduced, allowing the fitting of larger models with over 70 million trainable parameters, and large batch sizes.

A learning rate scheduling approach, reducing the base learning rate as a function of the number of workers followed by an exponential decay on a per-epoch basis is introduced to facilitate neural network convergence when training on HPC clusters with up to $O(100)$ worker GPUs.

Scalar multiplier α applied to the loss function before evaluating partial derivatives during the **bprop** step is found to be crucial for the model convergence at half-precision.

A Datasets

A.1 JET

We present a summary of the JET dataset [10] used throughout this paper. JET is the largest tokamak fusion experiment operating today and is situated in the UK. Plasma discharges (“shots”) range in length from ~ 1 to ~ 40 seconds and are sampled at a rate of 1 ms. Thus, there are $O(10^3)$ to $O(10^4)$ timesteps per shot. Each shot consists of a scalar floating point value for each of the following measured plasma parameters for each timestep:

1. q_{95} plasma safety factor
2. β : plasma beta
3. I_p : plasma current
4. l_i : plasma internal inductance
5. n : plasma number density

Signal	Test AUC	Train AUC	Val. AUC
Normalized Beta	0.5340	0.5249	0.4939
Locked mode amplitude	0.7503	0.7819	0.7765
Input Power	0.4158	0.4527	0.4538
Radiated Power Core	0.3597	0.3732	0.3902
Radiated Power Edge	0.6122	0.5933	0.6410
q95 safety factor	0.7914	0.7693	0.7838
Input Beam Torque	0.5284	0.5406	0.5242
Plasma density	0.5903	0.5817	0.5763
Electron dens. profile	0.7008	0.6976	0.7647
stored energy	0.6389	0.6518	0.6169
Electron temp. profile	0.7142	0.7226	0.7648
plasma current	0.7143	0.7017	0.7128
plasma current direct.	0.4787	0.4940	0.5221
plasma current error	0.4668	0.4652	0.4674
plasma current target	0.7757	0.7477	0.7465
internal inductance	0.3609	0.4026	0.3741

Table 2: Single signal summary for D3D dataset in terms of best validation level AUC, train and test level AUCs.

6. MLA : amplitude of the locked mode signal
7. P_{rad} : radiated power
8. E_{int} : internal energy
9. $\frac{\partial E_{int}}{\partial t}$: time derivative of internal energy
10. P_{in} : input power

A fraction of about 10% of shots ends in a disruption. These shots are referred to as disruptive. All other shots are called non-disruptive.

The dataset consists of ~ 4300 shots from JET experimental campaigns C15-C27b. During these campaigns the JET tokamak had carbon fiber composite (CFC) walls. These shots are used for training and validation in an 80/20 split. The dataset also includes and ~ 1100 shots from the campaigns C28-30. In these more recent campaigns, the tokamak was upgraded to have a moder modern metallic wall. These shots are used for testing.

A.2 Large Movie Review Dataset (IMDB)

The dataset contains movie reviews along with their associated binary sentiment polarity labels [1]. It often serves as a benchmark for sentiment classification. It contains 50000 reviews split evenly between train and test sets.

In the entire collection, no more than 30 reviews are allowed for any given movie because reviews for the same movie tend to have correlated ratings. Further, the train and test sets contain a disjoint set of movies. In the labeled train and test sets, a negative review has a score of less or equal to 4 out of 10, and a positive review has a score of greater or equal to 7 out of 10. Thus reviews with more neutral ratings are not included in the train/test sets.

References

- [1] Andrew L. Maas, Raymond E. Daly, Peter T. Pham, Dan Huang, Andrew Y. Ng, and Christopher Potts. Learning word vectors for sentiment analysis. In *Proceedings of the 49th Annual Meeting of the Association for Computational Linguistics: Human Language Technologies*, pages 142–150, Portland, Oregon, USA, June 2011. Association for Computational Linguistics.

Signal	Test AUC	Train AUC	Val. AUC
Normalized Beta	0.7805	0.8112	0.8074
Locked mode amplitude	0.7785	0.7492	0.7799
Input Power	0.7907	0.7933	0.7794
Radiated Power Core	0.7903	0.8311	0.7764
Radiated Power Edge	0.7891	0.7244	0.7794
q95 safety factor	0.6777	0.7228	0.7676
Input Beam Torque	0.7514	0.7868	0.7569
Plasma density	0.7966	0.7519	0.7370
Electron dens. profile	0.7976	0.7732	0.7716
stored energy	0.7873	0.7785	0.7835
Electron temp. profile	0.8069	0.7895	0.7850
plasma current	0.7993	0.7974	0.7829
plasma current direct.	0.8034	0.7731	0.7813
plasma current error	0.7439	0.7596	0.7742
plasma current target	0.7802	0.7991	0.7710
internal inductance	0.7461	0.7640	0.7694

Table 3: Augmented study summary for D3D dataset in terms of best validation level AUC, train and test level AUCs. During training, augment one signal at random, one at a time. During inference, augment a fixed signal, one at a time.

- [2] Jeffrey Dean, Greg Corrado, Rajat Monga, Kai Chen, Matthieu Devin, Mark Mao, Marc'aurelio Ranzato, Andrew Senior, Paul Tucker, Ke Yang, Quoc V. Le, and Andrew Y. Ng. Large scale distributed deep networks. In F. Pereira, C. J. C. Burges, L. Bottou, and K. Q. Weinberger, editors, *Advances in Neural Information Processing Systems 25*, pages 1223–1231. Curran Associates, Inc., 2012.
- [3] Alex Krizhevsky, Ilya Sutskever, and Geoffrey E Hinton. Imagenet classification with deep convolutional neural networks. In F. Pereira, C. J. C. Burges, L. Bottou, and K. Q. Weinberger, editors, *Advances in Neural Information Processing Systems 25*, pages 1097–1105. Curran Associates, Inc., 2012.
- [4] Sang Kyun Kim, Lawrence C McAfee, Peter Leonard McMahon, and Kunle Olukotun. A highly scalable restricted boltzmann machine fpga implementation. In *Field Programmable Logic and Applications, 2009. FPL 2009. International Conference on*, pages 367–372. IEEE, 2009.
- [5] Rafal Józefowicz, Oriol Vinyals, Mike Schuster, Noam Shazeer, and Yonghui Wu. Exploring the limits of language modeling. *CoRR*, abs/1602.02410, 2016.
- [6] Matthieu Courbariaux, Yoshua Bengio, and Jean-Pierre David. Training deep neural networks with low precision multiplications. *arXiv e-prints*, abs/1412.7024, December 2014.
- [7] Darryl D. Lin, Sachin S. Talathi, and V. Sreekanth Annapureddy. Fixed point quantization of deep convolutional networks. In *Proceedings of the 33rd International Conference on International Conference on Machine Learning - Volume 48*, ICML'16, pages 2849–2858. JMLR.org, 2016.
- [8] Itay Hubara, Matthieu Courbariaux, Daniel Soudry, Ran El-Yaniv, and Yoshua Bengio. Quantized neural networks: Training neural networks with low precision weights and activations. *arXiv e-prints*, abs/1609.07061, September 2016.
- [9] Martín Abadi, Ashish Agarwal, Paul Barham, Eugene Brevdo, Zhifeng Chen, Craig Citro, Greg S. Corrado, Andy Davis, Jeffrey Dean, Matthieu Devin, Sanjay Ghemawat, Ian Goodfellow, Andrew Harp, Geoffrey Irving, Michael Isard, Yangqing Jia, Rafal Jozefowicz, Lukasz Kaiser, Manjunath Kudlur, Josh Levenberg, Dan Mané, Rajat Monga, Sherry Moore, Derek Murray, Chris Olah, Mike Schuster, Jonathon Shlens, Benoit Steiner, Ilya Sutskever, Kunal Talwar, Paul Tucker, Vincent Vanhoucke, Vijay Vasudevan, Fernanda Viégas, Oriol Vinyals, Pete Warden, Martin Wattenberg, Martin Wicke, Yuan Yu, and Xiaoqiang Zheng. TensorFlow: Large-scale machine learning on heterogeneous systems, 2015. Software available from tensorflow.org.

- [10] Jesús Vega, Sebastián Dormido-Canto, Juan M López, Andrea Murari, Jesús M Ramírez, Raúl Moreno, Mariano Ruiz, Diogo Alves, Robert Felton, JET-EFDA Contributors, et al. Results of the jet real-time disruption predictor in the iter-like wall campaigns. *Fusion Engineering and Design*, 88(6):1228–1231, 2013.
- [11] Julian Kates-Harbeck, Alexey Svyatkovskiy, Kyle Felker, Eliot Feibush, and William Tang. Disruption forecasting in tokamak fusion plasmas using deep recurrent neural networks. *Manuscript in preparation*, 2017.
- [12] Felix A Gers, Jürgen Schmidhuber, and Fred Cummins. Learning to forget: Continual prediction with lstm. 1999.
- [13] Junhua Mao, Wei Xu, Yi Yang, Jiang Wang, Zhiheng Huang, and Alan Yuille. Deep captioning with multimodal recurrent neural networks (m-rnn). *ICLR*, 2015.
- [14] Richard Socher, Alex Perelygin, Jean Wu, Jason Chuang, Christopher D. Manning, Andrew Y. Ng, and Christopher Potts. Recursive deep models for semantic compositionality over a sentiment treebank. In *Proceedings of the 2013 Conference on Empirical Methods in Natural Language Processing*, pages 1631–1642, Stroudsburg, PA, October 2013. Association for Computational Linguistics.
- [15] Ilya Sutskever, Oriol Vinyals, and Quoc V Le. Sequence to sequence learning with neural networks. In Z. Ghahramani, M. Welling, C. Cortes, N. D. Lawrence, and K. Q. Weinberger, editors, *Advances in Neural Information Processing Systems 27*, pages 3104–3112. Curran Associates, Inc., 2014.